Numerical Investigation of Multiphase Flow through Complex Fractures

Prakash Purswani[1,*], Javier E. Santos[1], Jeffrey D. Hyman[1], and Eric J. Guiltinan[1]

[1]Earth and Environmental Sciences Division, Los Alamos National Laboratory, Los Alamos, NM, 87545

[*]Corresponding author: Prakash Purswani, ppurswani@lanl.gov

Abstract

Multiphase flow through fractures has great significance in subsurface energy recovery and gas storage applications. Different fracture and flow properties affect flow through a fracture which is difficult to control in laboratory experiments. Here, we perform lattice Boltzmann simulations in an ensemble of synthetically generated fractures. Drainage simulations are performed at different capillary numbers, wettability, and viscosity ratios. We track the invading front and quantify breakthrough saturations and show that roughness and wettability have a profound effect on fluid invasion through a complex fracture. Invading a more viscous fluid results in more stable displacement regardless of the capillary number while at very low capillary numbers, fluid migration is dependent on the inherent structure of the fracture. Through a systematic investigation, we develop fluid displacement phase diagrams across multiple fractures, and demonstrate the importance of natural fracture features of roughness and wettability in establishing stable versus unstable displacement during multiphase flow.

Plain-level Summary—

In this research, we perform multiphase flow simulations through single fractures. We assess the movement of the invading fluid by varying different physical attributes of the fractured media as well as by varying the different fluid flow conditions. Through numerical simulations, we establish strict control on these attributes such that their impact on flow dynamics can be studied independently which is not possible through experiments. Fluid invasion is studied through quantitative metric of fluid invasion front and breakthrough saturations. We show that the dynamics of fluid movement through fractured media is highly sensitive to fracture properties of surface roughness as well as to the flow properties of capillary numbers, wettability, and viscosity ratios.

Keywords— Multiphase flow, fluid flow through fractures, Lattice Boltzmann simulations, surface roughness, wettability, capillary number, viscosity ratio

Highlights—

- High-fidelity multiphase flow numerical simulations are performed through single rough-walled fractured media.
- A variety of fracture and flow parameters are tested including surface roughness, wettability, viscosity ratios, and capillary numbers.
- Invading phase front and breakthrough saturations are quantified for the different conditions and phase diagram with stable and unstable displacement regimes are plotted.
- Displacement regimes are analyzed for a variety of different fracture realizations, and it is shown that the displacement regimes are highly sensitive to the inherent fracture properties.

1 Introduction

Fluid flow through fractures is of great importance for a variety of geoscience applications pertaining to energy and the environment. Energy applications include safe and long-term geologic carbon sequestration, zero-carbon technologies like geologic hydrogen storage, and hydraulic fracturing for hydrocarbon production Khosravi et al. (2014), Wang et al. (2022), March et al. (2018), Hussain et al. (2021) while environmental applications include secure disposal of nuclear waste and remediation of contaminated groundwater Birkholzer et al. (2012), Ghanbarzadeh et al. (2015), Zhou et al. (2023). Fractures are high-conductive pathways that control most of the flow through tight geologic media where matrix porosities and permeabilities are in the ultra-low range. Fractures are complex and highly heterogeneous with variation both at the small- and large-scale. At the small-scale (mm-cm scale) heterogeneity arises due to fracture aperture distributions/mean apertures, surface roughness, and aspect ratios whereas at the large-scale (m-km scale), fracture lengths, connectivity, and the orientation of the connected fracture govern transport Hyman et al. (2015, 2021), Song et al. (2023). The two scales are inherently interlinked where local heterogeneities directly influence transport at the larger scale. In this research, we focus at the small-scale to investigate the impact of various fracture and flow parameters on the dynamics of multiphase fluid flow through single rough-walled complex fractures.

Sophisticated experimental techniques such as x-ray microcomputed tomography (μCT) have enabled digital characterization of fracture properties. Bertels et al. (2001) performed steady-state experiments using x-ray μCT in a fractured basalt sample to study the impact of fracture aperture distribution (mean aperture of 336 μm) on phase saturations. During flooding, they measured relative permeabilities and capillary pressures and showed that relative permeabilities are not linear for a gas-water system during flow through a rough-walled fracture and that there was significant retention of water (as the wetting phase) in the fracture. Similarly, Karpyn et al. (2007) performed experiments in a single rough-walled fracture in a Berea sandstone to visualize and quantify fluid occupancy using μCT. Mechanisms of capillary trapping of the nonwetting phase and by-passing flow of the wetting phase were captured through quantitative image analysis. Importance of fracture aperture and presence of local heterogeneity in the rough surface was found to be critical for phase trapping. Chen, Wu, Fang & Hu (2018) performed experiments to study displacement regimes in a single rough-walled fracture for different capillary numbers and viscosity ratios. The experiments were performed for a water/glycerol mixture displacing silicone oil where the invading fluid contact angle was $\approx 161^{\circ}$. They generated a phase diagram by plotting contours for the nonwetting phase breakthrough saturations and found spatial variability of the fracture domain to cause unstable displacement efficiency. They also found that fluid migrated with a stable displacement in the fracture until some variability was reached, after which fingering was observed. Such flow experiments provide valuable insights regarding fracture and flow attributes; however, these are often cumbersome and yield displacement information for a single fracture. Sophisticated numerical techniques are therefore often used to supplement experimental works.

Dou et al. (2013) performed lattice Boltzmann method (LBM) simulations in a self-affine fracture to study the effect of wettability on the evolution of fluid-fluid interfacial area during invading phase flow through the fracture. The nonwetting phase was found to flow through larger openings in the fracture. They found a nonlinear trend of fluid-fluid interfacial area with the invasion of the nonwetting phase with a maximum at a water saturation of ≈0.2. Similar trends have been observed for traditional water-wet porous media through experimental Culligan et al. (2004, 2006) and simulation work (Reeves & Celia (1996), Landry et al. (2014), McClure et al. (2018)). Guiltinan et al. (2021) also performed LBM simulations in rough-walled synthetic fractures to study CO_2-brine migration through the fracture. They developed an interface tracking approach for estimating relative permeabilities for such a system involving transient flow and found the dynamics of CO_2 migration through the fracture to be significantly impacted by local aperture and wettability variations in the fracture. Other reports have also demonstrated the importance of wettability through a combination of experimental and simulation work and have extended the traditional displacement phase diagram in the capillary number-viscosity ratio-wettability space Zhao et al. (2016), Lan et al. (2020), Primkulov et al. (2019, 2021). Similarly, the effect of surface roughness has been shown to be critical to fluid displacement through fracture Chen, Wu, Fang & Hu (2018), Yi et al. (2019), Hu et al. (2019).

Overall, in the literature, there is breadth of experimental and numerical works that study multiphase flow through complex fractures. Further, it is established that different fracture attributes as well as flow properties govern fluid flow through complex fractures. However, there is no study that provides a comprehensive analysis where effects of both flow and fracture properties is considered holistically. In this research, we aim to bridge this gap by taking a systematic approach for quantifying the effect of various flow and fracture parameters on the flow of invading fluid through complex rough-walled fractures. We implement state-of-the-art numerical fracture generation technique called pySimFrac Guiltinan et al. (2023) and direct numerical simulation technique called MF-LBM Chen, Li, Valocchi & Christensen (2018), Chen et al. (2019) to investigate these scenarios and report our findings for different realistic fracture realizations. We first describe these techniques in Section 2 and describe the simulations sets considered. In Section 3, we discuss the results characterizing the dynamics of fluid invasion for different fracture (Hurst exponent and root mean squared (rms) roughness) and flow parameters (capillary numbers and contact angles) and lastly, we describe the effect of these properties in combination with different viscosity ratios.

2 Methodology

2.1 Description of fracture generation and numerical simulations

We utilized pySimFrac, a new python-based library, to numerically generate realistic single fracture realizations Guiltinan et al. (2023). In addition to fracture generation, we utilized extended capabilities within pySimFrac to perform direct numerical multiphase simulations through the fractures. PySimFrac offers two numerical methods for fracture generation, namely, convolution and spectral-based methods. We used the spectral method for generating the fractures. This method is an extension of the Brown method where three inputs are required to develop a numerical fracture, namely, the rms roughness, mismatch between the fracture surfaces, and the fractal dimension Brown (1995). The updated spectral method offers additional capabilities such as the aspect ratio, fracture seed, as well as the correlation length Glover et al. (1998*a*,*b*, 1999), Ogilvie et al. (2006). Here, we vary fracture seed, rms roughness, and the Hurst exponent to study the effect of fracture surface variability on flow. The Hurst exponent is related to the fractal dimension Babadagli et al. (2015) which is a measure of the surface texture. It ranges between zero and one with larger Hurst exponent relating to smaller fractal dimension and producing smoother fractures. The rms roughness parameter, however, calibrates roughness by controlling the standard deviation of the heights of the fracture surfaces. It scales between zero and infinity with zero referring to a completely smooth surface and has units of length. The mean aperture of the fractures generated in this study was fixed at 15 lattice units (lus) which would correspond to 3.3 μm/lu for a fracture with mean aperture of 50 μm commonly observed for natural fractures in Barnett Shale Gale et al. (2007), Guiltinan et al. (2021).

For the direct numerical multiphase simulations, we used an LBM code, MF-LBM, developed at the Los Alamos National Laboratory (LANL) Chen, Li, Valocchi & Christensen (2018), Chen et al. (2019) (`https://github.com/lanl/mf-lbm`). MF-LBM is a highly-parallelized code that allows for faster execution with GPU-enabled computing resources. The code is developed using the continuum-surface-force combined color-gradient (CSF-CD) scheme for delineating the two phases Brackbill et al. (1992), Xu et al. (2017). Furthermore, MF-LBM uses the geometrical wetting model and the multi relaxation time (MRT) framework for simulating two-phase flow effectively Leclaire et al. (2016, 2017), d'Humières et al. (2002), Akai et al. (2018). It has been benchmarked against CO_2 displacement experiments conducted in a 2-D heterogeneous micromodel Chen, Li, Valocchi & Christensen (2018). In MF-LBM we input flow and rock/fluid interaction parameters including contact angles, capillary numbers, viscosity ratios, and interfacial tension. All simulations were analyzed until the breakthrough point of the invading phase. The simulations were executed on the Nvidia A100 GPU partition of the Chicoma supercomputer at LANL (`https://www.lanl.gov/org/ddste/aldsc/hpc/index.php`). The time required to run the simulations depended on different factors including the input capillary number and how extreme or simple the fracture and flow properties were to the flow of the invading phase causing faster or slower breakthrough of the invading phase. As an example, the time required to complete the different simulations for different capillary numbers is shown in Figure S1.

2.2 Description of simulation cases

Table 1 summarizes the different fracture and flow parameters considered in this work. For the fracture parameters, Hurst exponent and rms roughness were considered. We considered these for three fracture seeds. For flow parameters, we considered contact angles (reported against the defending phase), capillary numbers ($N_{ca} = \mu_i U/\sigma$) and viscosity ratio ($M = \mu_i/\mu_d$), where U is the Darcy velocity, σ is the fluid-fluid interfacial tension, and μ_i and μ_d are the viscosities of the invading and defending phases, respectively. All parameter ranges were tested thoroughly to arrive at these numbers to prevent numerical instabilities that could occur with the LBM simulator under extreme values. We coupled the analysis of viscosity ratios together with capillary numbers to study different displacement regimes of the invading phase. With these cases, we were able to investigate a broad range of flow and fracture properties to study their impact on the dynamics of multiphase flow.

Table 1: Summary of the different fracture and flow parameters and their range tested in this research.

Parameter	**Values tested**	**Units**
Rms roughness	[1, 2, 3, 4, 5, 6]	[l]
Fracture seed	[1, 2, 3]	[-]
Hurst exponent	[0.1, 0.2, 0.3, 0.4, 0.5, 0.6, 0.7, 0.8, 0.9, 0.95]	[-]
Contact angle	[10, 30, 50, 70, 90, 110]	[°]
Capillary number	[5^{-1}, 1^{-1}, 5^{-2}, 1^{-2}, 5^{-3}, 1^{-3}, 5^{-4}, 1^{-4}, 5^{-5}, 1^{-5}, 5^{-6}]	[-]
Invading phase viscosity	[0.004, 0.04, 0.2]	LBM units
Receding phase viscosity	[0.004, 0.04]	LBM units
Viscosity ratio	[10.0, 1.0, 0.1, 0.02]	[-]

3 Results and discussion

3.1 Dynamics of multiphase flow through single fracture media

Figure 1 shows the breakthrough saturation (BTS) for different fracture and flow parameters. Here, we observe that as Hurst exponent decreases, the BTS decreases, showing that the displacement is relatively unstable whereas at larger Hurst exponents, the BTS values are larger (stable displacement) owing to less roughness. Note that at the largest value of Hurst exponent, breakthrough still occurred at a value less than one, owing to flow controlled by the rms roughness parameter. With larger rms roughness, the BTS is affected significantly. A nearly linear trend is observed here for the range of rms roughness tested.

It is useful to note that when setting simulations for the Hurst exponent (Figure 1a), surface roughness, contact angle, and capillary numbers were set to 4, 45°, and 10^{-4}, respectively. Similarly, for simulations to test surface roughness (Figure 1b), capillary number and contact angle were set as previously, while Hurst exponent was set at 0.7. For contact angle cases (Figure 1c), Hurst exponent, surface roughness, and capillary number were set at 0.7, 4, and 10^{-4}, respectively. Lastly, for the capillary number cases (Figure 1d), Hurst exponent, surface roughness, and contact angle were set at 0.7, 4, and 45°, respectively. In addition, the viscosity ratio between invading and receding phase was set at 1.0 throughout the cases discussed in Figure 1. The parameter values set here were arrived at after intensive testing to keep the fixed attributes in the middle of their respective ranges so as not to have their impact dominate flow.

From Figure 1c we find that wettability has a significant impact on the flow of fluids inside the fracture. At low contact angles, the invading phase is nonwetting to the medium and has an unstable displacement with BTS as low as 0.5, whereas when the invading phase is weakly- to neutral nonwetting, the front moves stably through the fracture. Similar findings for the effect of wettability have been shown through multiphase experiments in 2D microfluidic cell where compact displacement of the invading phase was observed around neutral wettability Zhao et al. (2016). Capillary number, similarly, shows a strong impact on fluid invasion through the fracture. As expected, lower capillary numbers led to more stable displacements and vice versa (Figure 1d). We provide a detailed analysis on the role of capillary number in Figure 2.

The right column in Figure 1 shows the progression of the invading front into the fracture plotted against the saturation of the invading phase for the different cases discussed in the left column of Figure 1. The length of the invading front is normalized against the entire length of the fracture (512 lus). For all properties tested, a range of behavior is observed from faster to slower progression of the invading front. The impact of local heterogeneity can be captured here through irregular movement of the invading front. Stable displacement falls near the y = x line on the plot. Both Hurst exponent and rms roughness led to faster movement of the invading front. Similarly, strong nonwetting behavior of the invading fluid as well as higher capillary numbers led to unstable displacement. For the Hurst exponent, the value of 0.7, marked a transition in the profile of the invading front. Similarly, stable displacement threshold for rms roughness was found at $<= 3.0$. For contact angles, stable displacement threshold was found to be at $>= 70°$. Lastly, for capillary numbers, stable displacement threshold was found to be at 10^{-3}. The step-like nature of the front progression reveals the presence of capillary fingering Tsuji et al. (2016), Bakhshian et al. (2019), visible for cases with Hurst exponent, rms roughness $>= 3.0$, and contact angle $>= 50°$, while viscous fingering was observed for capillary number $>= 5x10^{-3}$.

Overall, BTS values are not observed to be below 0.5 in all cases tested here. We find that cases with Hurst exponent shows larger variance with the fracture seed and less variation in the BTS values [≈0.65-0.8] across the different hurst exponent. Comparatively, other properties show at least a 0.3-unit difference in the observed BTS values. This suggests that Hurst exponent as a parameter has less effect on the displacement regime of the invading fluid. Particularly, the impact of contact angle and rms roughness is the most evident and their effect is explored in more detail in the following sections.

3.2 Displacement patterns across a single complex fracture

Figure 2 shows the breakthrough saturation and invading fluid progression through the exact same fracture for different viscosity ratios and capillary numbers. In developing this fracture realization rms roughness and Hurst exponent, were fixed at 4 and 0.7, respectively, while the seed was set at one. In addition, for these simulations, contact angle was set to 45°. Only viscosity ratios (10.0, 1.0, 0.1, and 0.02) and capillary numbers (ranging from 5×10^{-2} to 5×10^{-6}) were varied. Note that for viscosity ratios of 0.1 and 0.02, at very high capillary numbers of 5×10^{-2}, simulations failed to complete till the breakthrough point due to velocity-caused numerical instabilities in the simulator and, therefore, these data points are not available for comparison. Nevertheless, the wide range of capillary numbers tested provide meaningful data to make useful comparisons.

From Figure 2a, it is observed that the behavior of flow is highly dependent on the flow conditions. For higher viscosity ratio (10.0), the flow of invading phase is stable and the BTS is less impacted by capillary number, meaning regardless of the input velocity change, the invading front progresses through the fracture remained the same (Figure 2b), where the fronts fall near the y=x line. For the viscosity ratio of one (Figure 2a blue curve), invading phase is dependent on the capillary number. This was previously discussed in Section 3.1. (Figure 1d). Finally, for the lower viscosity ratios (0.1 and 0.02), where the invading phase is less viscous, the dependence of the movement of the invading phase on flow velocity is further enhanced. The BTS values for this case change significantly ranging from ≈0.42-0.85. A steep linear dependence is found between capillary number on the log-scale and BTS. Viscosity ratio of 1.0 is found to be a transition case where both constant BTS and linear changes in BTS with capillary number is found. For viscosity ratios $<= 1.0$, higher capillary number led to faster breakthroughs, while lower capillary numbers, the movement of front becomes more stable (Fig. S2 c, d and e) leading to larger BTS values. At the limit of very low capillary numbers, the dependence on viscosity ratios minimizes and BTS is controlled by the inherent fracture property (input of rms roughness).

We develop a phase diagram in Figure 2b to describe different displacement regimes from the data in Figure 2a. It is conceptualized through a contour map of BTS values of the invading phase to assess the stability of a displacement regime. The faster the BTS, more unstable the displacement and vice versa. This is plotted on a mesh of capillary numbers and viscosity ratios similar to the experimental work of Chen et al.

(2017), Chen, Wu, Fang & Hu (2018). The data points that were unavailable due to numerical instabilities were set to the last available data point. With viscosity ratios between 0.02 to 10, we focus in the transition zone between viscous and capillary regimes as seen from the traditional Lenormand diagram Lenormand et al. (1988), Lenormand & Zarcone (1984) that was developed through simplified pore-network experiments Lenormand et al. (1983). One reason is that the transition zone is not well explored in the literature, especially for flow through complex fractures and also that these viscosity ratios (0.1 and 0.02) are relevant for physical systems representative of CO_2-water as well as H_2-water injection for the purposes of geological gas storage Herring et al. (2016), Chen et al. (2019), Delshad et al. (2022). We find that lower capillary numbers result in stability of flow for all viscosity ratios. At larger capillary numbers, however, the stability is strongly dependent on viscosity ratios, moving from the most unstable at low viscosity ratios to the most stable at high viscosity ratios. At viscosity ratio of 10.0, the flow is stable across most capillary numbers, with a slightly more stable zone around intermediate capillary numbers because around that zone, flow is controlled by the geometry of the flow domain dependent on the fracture properties. On the contrary, at low viscosity ratios, flow is mostly unstable across all capillary numbers, but becomes increasingly unstable as capillary numbers increases. Overall, the most unstable zone is found at high capillary numbers and low viscosity ratios, while the most stable zone is found at high viscosity ratios and intermediate capillary numbers. We overlay the boundaries of capillary fingering (bounded by the viscosity ratio axis), viscous fingering (bounded by the capillary number axis), and stable displacement (top-right corner) for traditional porous media Lenormand et al. (1988), Zhang et al. (2011) and for a single rough fracture Chen, Wu, Fang & Hu (2018). We find that in a single rough fracture the change in BTS values is significant ranging from $\approx$0.3 to 0.9 even when operating in the transition zone of the different displacement regimes making the boundary definition from Lenormand et al. (1988) less applicable. However, the boundaries as described in Zhang et al. (2011), Chen, Wu, Fang & Hu (2018) show a narrower representation of the transition zone slightly more representative of the observation from our simulations. In the next section, we extend this discussion across multiple rough fractures.

3.3 Displacement patterns across multiple complex fractures

In Figure 3 we describe displacement phase diagrams across different complex fractures whose rms roughness (2, 4, and 6) and wettability (30°, 50°, and 70°) are varied. Additional information for these fracture surface properties and corresponding dimensionless roughness parameters are given in Table S1 and the simulation data used to construct the phase diagrams are shown in Figure S3. As phase becomes more nonwetting, keeping viscosity ratios fixed, a delayed breakthrough is observed. Similarly, as the fracture becomes rough, there is a significant impact on BTS. At low roughness, the effect of capillary number is observed for viscosity ratios of 0.1 and 0.02. Even here for low capillary numbers, lower than 10^{-4}, leads to almost stable flow with much delayed breakthroughs (black contour line). The worst case is observed for $\theta = 30°$and roughness of 6, where breakthroughs range between 0.3 and 0.7. Effect of capillary number is seen more clearly for the case of roughness of 4 when viscosity ratios are 0.02 and 0.1. Here, nearly linear trend is seen with capillary number on log-scale (Figure S3) and the slope of the linear trend is found to be a dependent on wettability. Similarly, effect of wettability is found to be significant when roughness is 6. Despite such high roughness, for viscosity ratio of 10.0 and contact angle of 70°, BTS values are > 0.9, showing stable displacement. In addition, all phase diagrams convey that at very low capillary number, the BTS tend to converge to a single value. This value can be as high as 1.0 (low rms roughness and high contact angle) to $\approx$0.5 (high rms roughness and low contact angle) reinforcing that the inherent characteristic of the fracture ultimately govern the nature of fluid invasion through the fracture.

Phase diagrams for very low viscosity ratios were developed for wettability against capillary number (Lan et al. (2020)) and between roughness and capillary number (Hu et al. (2019)) through experiments, simulations, and theoretical models. Our trends show general agreement such that the more nonwetting and the lower the capillary number, more stable the displacement front; and that more smooth the fracture and the lower the capillary number, more stable the displacement. In addition, these trends persists for most viscosity ratio, however, the evolution of the stability of the displacement regime is found to be a function of all contributing parameters: roughness, wettability, viscosity ratios, and capillary number. This helps us appreciate that such displacement regimes can be significantly different from one fracture to another and that such generalizations should be made with caution. This is for the first time that a representation of phase volume (instead of traditional phase diagrams) delineating stable versus unstable displacement for flow through complex fractures has been presented. In our future work, we will extend the analysis to quantify transport through averaged properties such as permeability and relative permeability.

4 Conclusions

In this letter, we describe direct numerical multiphase simulations in different single fracture realizations to study the impact of various fracture and flow parameters on the dynamics of invading fluid flow. For fracture parameters, we vary the fracture seed and fracture roughness by varying the Hurst exponent and the rms roughness parameter. For the flow, we test the effect of fracture wettability, capillary number, and viscosity ratio. The simulations were performed using a high-fidelity physics-based lattice Boltzmann simulator. The following conclusions are drawn:

- Hurst exponent, rms roughness, and wettability influence the dynamics of the invading phase flow through the fracture. At low rms roughness, the invading phase migrates through the fracture in a piston-like fashion while at larger values, sharper breakthroughs ($\approx$0.6) are observed. For strong nonwetting conditions (contact angle 10°), the invading phase breaks through at $\approx$0.5 saturation, while at neutral wettability, the invading phase flows as a piston-like regime.
- For a single rough fracture, at low capillary numbers, the invading phase moves such that the BTS is constrained by the fracture properties, regardless of the viscosity ratio. At high capillary numbers, however, viscosity ratios significantly affect the movement of the invading phase when the viscosity ratio are equal or unfavorable.
- Fluid displacement phase diagrams show that the viscosity ratios considered here fall within the cross-over zone of the traditional Lenormand-type phase diagram and even within the cross-over zone, displacement patterns are quite different when roughness and wettability attributes are varied. We demonstrate that flow in fractured media cannot be described by a single flow regime phase diagram and is instead specific to the fracture and flow conditions considered. Unlike traditional phase diagrams, a phase volume across fracture roughness and wettability is developed to describe stable versus unstable displacement regimes for multiphase flow through complex fractures.

Nomenclature

χ Normalized front tip length

$\mu\ CT$ Microcomputed tomography

μ_d Defending fluid viscosity

μ_i Invading fluid viscosity

σ Fluid-fluid interfacial tension

θ Contact angle measured through the receding phase

BTS Breakthrough saturation

LBM Lattice Boltzmann method

lu Lattice unit

M Viscosity ratio

Nca Capillary number

U Darcy velocity

Data Availability Statement

All of the data discussed in the paper is archived and available at `https://zenodo.org/record/8247637`.

Software Availability Statement

Synthetic fractures were generated using the pySimFrac toolkit available at `https://github.com/lanl/dfnWorks/tree/pysimfrac/pysimfrac` Guiltinan et al. (2023). The multiphase simulations in this research were performed using the MF-LBM code available at `https://github.com/lanl/mf-lbm` Chen et al. (2019) distributed under the BSD-3 license. The extracted data from the simulation presented in this research was processed using 1) MS-Excel (version 2306) for data analysis and generating simple plots; 2) ParaView for the visualization of the front movement (ParaView version 5.11.0) available at `https://www.paraview.org/` Ahrens et al. (2005), Ayachit (2015); and 3) matplotlib for plotting the breakthrough saturation contour plots in the paper available at `https://matplotlib.org/`.

Acknowledgement

Research presented in this article was supported by the Laboratory Directed Research and Development program of Los Alamos National Laboratory under project number XXKF00 & XXFT00 and has been designated with the Los Alamos Unlimited Release number LA-UR-23-29351. J.E.S. would like to thank the Center for Nonlinear Studies for support. J.D.H. acknowledges support from the Department of Energy (DOE) Basic Energy Sciences program (LANLE3W1) for support. The research was supported as part of the Center on Geo-process in Mineral Carbon Storage, an Energy Frontier Research Center funded by the U.S. Department of Energy (DOE), Office of Science, Basic Energy Sciences (BES), under award # DE-SC0023429. This work has been partially funded by the Spent Fuel and Waste Science and Technology (SFWST) Campaign of the U.S. Department of Energy Office of Nuclear Energy. The views expressed in the article do not necessarily represent the views of the U.S. Department of Energy or the United States Government.

References

1. Ahrens, J. P., Geveci, B. & Law, C. C. (2005), Paraview: An end-user tool for large-data visualization, *in* 'The Visualization Handbook'.
   URL: *https://api.semanticscholar.org/CorpusID:56558637*

2. Akai, T., Bijeljic, B. & Blunt, M. J. (2018), 'Wetting boundary condition for the color-gradient lattice boltzmann method: Validation with analytical and experimental data', *Advances in Water Resources* **116**, 56–66.
   URL: *https://www.sciencedirect.com/science/article/pii/S030917081731028X*

3. Ayachit, U. (2015), *The ParaView Guide: A Parallel Visualization Application*, Kitware, Inc., Clifton Park, NY, USA.

4. Babadagli, T., Raza, S., Ren, X. & Develi, K. (2015), 'Effect of surface roughness and lithology on the water–gas and water–oil relative permeability ratios of oil-wet single fractures', *International Journal of Multiphase Flow* **75**, 68–81.
   URL: *https://www.sciencedirect.com/science/article/pii/S0301932215001226*

5. Bakhshian, S., Hosseini, S. A. & Shokri, N. (2019), 'Pore-scale characteristics of multiphase flow in heterogeneous porous media using the lattice boltzmann method', *Scientific Reports* **9**(1), 1–13.
   URL: *https://doi.org/10.1038/s41598-019-39741-x*

6. Bertels, S. P., DiCarlo, D. A. & Blunt, M. J. (2001), 'Measurement of aperture distribution, capillary pressure, relative permeability, and in situ saturation in a rock fracture using computed tomography scanning', *Water Resources Research* **37**(3), 649–662.
   URL: *https://agupubs.onlinelibrary.wiley.com/doi/abs/10.1029/2000WR900316*

7. Birkholzer, J., Houseworth, J. & Tsang, C.-F. (2012), 'Geologic disposal of high-level radioactive waste: Status, key issues, and trends', *Annual Review of Environment and Resources* **37**(1), 79–106.
   URL: *https://doi.org/10.1146/annurev-environ-090611-143314*

8. Brackbill, J., Kothe, D. & Zemach, C. (1992), 'A continuum method for modeling surface tension', *Journal of Computational Physics* **100**(2), 335–354.
   URL: *https://www.sciencedirect.com/science/article/pii/002199919290240Y*

9. Brown, S. R. (1995), 'Simple mathematical model of a rough fracture', *Journal of Geophysical Research: Solid Earth* **100**(B4), 5941–5952.
   URL: *https://agupubs.onlinelibrary.wiley.com/doi/abs/10.1029/94JB03262*

10. Chen, Y.-F., Fang, S., Wu, D.-S. & Hu, R. (2017), 'Visualizing and quantifying the crossover from capillary fingering to viscous fingering in a rough fracture', *Water Resources Research* **53**(9), 7756–7772.
URL: *https://agupubs.onlinelibrary.wiley.com/doi/abs/10.1002/2017WR021051*

11. Chen, Y.-F., Wu, D.-S., Fang, S. & Hu, R. (2018), 'Experimental study on two-phase flow in rough fracture: Phase diagram and localized flow channel', *International Journal of Heat and Mass Transfer* **122**, 1298–1307.
URL: *https://www.sciencedirect.com/science/article/pii/S0017931017354832*

12. Chen, Y., Li, Y., Valocchi, A. J. & Christensen, K. T. (2018), 'Lattice boltzmann simulations of liquid co2 displacing water in a 2d heterogeneous micromodel at reservoir pressure conditions', *Journal of Contaminant Hydrology* **212**, 14–27.
URL: *https://www.sciencedirect.com/science/article/pii/S0169772217300645*

13. Chen, Y., Valocchi, A. J., Kang, Q. & Viswanathan, H. S. (2019), 'Inertial effects during the process of supercritical co2 displacing brine in a sandstone: Lattice boltzmann simulations based on the continuum-surface-force and geometrical wetting models', *Water Resources Research* **55**(12), 11144–11165.
URL: *https://agupubs.onlinelibrary.wiley.com/doi/abs/10.1029/2019WR025746*

14. Culligan, K. A., Wildenschild, D., Christensen, B. S. B., Gray, W. G., Rivers, M. L. & Tompson, A. F. B. (2004), 'Interfacial area measurements for unsaturated flow through a porous medium', *Water Resources Research* **40**(12).
URL: *https://agupubs.onlinelibrary.wiley.com/doi/abs/10.1029/2004WR003278*

15. Culligan, K., Wildenschild, D., Christensen, B., Gray, W. & Rivers, M. (2006), 'Pore-scale characteristics of multiphase flow in porous media: A comparison of air–water and oil–water experiments', *Advances in Water Resources* **29**(2), 227–238. Experimental Hydrology: A Bright Future.
URL: *https://www.sciencedirect.com/science/article/pii/S030917080500120X*

16. Delshad, M., Umurzakov, Y., Sepehrnoori, K., Eichhubl, P. & Batista Fernandes, B. R. (2022), 'Hydrogen storage assessment in depleted oil reservoir and saline aquifer', *Energies* **15**(21).
URL: *https://www.mdpi.com/1996-1073/15/21/8132*

17. d'Humières, D., Ginzburg, I., Krafczyk, M., Lallemand, P. & Luo, L.-S. (2002), 'Multiple-relaxation-time lattice boltzmann models in three dimensions', *Philosophical Transactions of the Royal Society of London. Series A: Mathematical, Physical and Engineering Sciences* **360**(1792), 437–451.
URL: *https://royalsocietypublishing.org/doi/abs/10.1098/rsta.2001.0955*

18. Dou, Z., Zhou, Z. & Sleep, B. (2013), 'Influence of wettability on interfacial area during immiscible liquid invasion into a 3d self-affine rough fracture: Lattice boltzmann simulations', *Advances in Water Resources* **61**, 1–11.
URL: *https://www.sciencedirect.com/science/article/pii/S0309170813001462*

19. Gale, J. F. W., Reed, R. M. & Holder, J. (2007), 'Natural fractures in the Barnett Shale and their importance for hydraulic fracture treatments', *AAPG Bulletin* **91**(4), 603–622.
URL: *https://doi.org/10.1306/11010606061*

20. Ghanbarzadeh, S., Hesse, M. A., Prodanović, M. & Gardner, J. E. (2015), 'Deformation-assisted fluid percolation in rock salt', *Science* **350**(6264), 1069–1072.
URL: *https://www.science.org/doi/abs/10.1126/science.aac8747*

21. Glover, P., Matsuki, K., Hikima, R. & Hayashi, K. (1998*a*), 'Fluid flow in synthetic rough fractures and application to the hachimantai geothermal hot dry rock test site', *Journal of Geophysical Research: Solid Earth* **103**(B5), 9621–9635.

22. Glover, P., Matsuki, K., Hikima, R. & Hayashi, K. (1998*b*), 'Synthetic rough fractures in rocks', *Journal of Geophysical Research: Solid Earth* **103**(B5), 9609–9620.

23. Glover, P., Matsuki, K., Hikima, R. & Hayashi, K. (1999), 'Characterizing rock fractures using synthetic fractal analogues', *Geothermal science and technology* **6**(1-4), 83–112.

24. Guiltinan, E. J., Santos, J. E., Cardenas, M. B., Espinoza, D. N. & Kang, Q. (2021), 'Two-phase fluid flow properties of rough fractures with heterogeneous wettability: Analysis with lattice boltzmann simulations', *Water Resources Research* **57**(1), e2020WR027943.
URL: *https://agupubs.onlinelibrary.wiley.com/doi/abs/10.1029/2020WR027943*

25. Guiltinan, E. J., Santos, J. E., Purswani, P. & Hyman, J. D. (2023), 'Pysimfrac: A python library for synthetic fracture generation, analysis, and simulation', *Computaters & Geosciences* **Submitted**.

26. Herring, A. L., Andersson, L. & Wildenschild, D. (2016), 'Enhancing residual trapping of supercritical co2 via cyclic injections', *Geophysical Research Letters* **43**(18), 9677–9685.
URL: *https://agupubs.onlinelibrary.wiley.com/doi/abs/10.1002/2016GL070304*

27. Hu, R., Zhou, C.-X., Wu, D.-S., Yang, Z. & Chen, Y.-F. (2019), 'Roughness control on multiphase flow in rock fractures', *Geophysical Research Letters* **46**(21), 12002–12011.
URL: *https://agupubs.onlinelibrary.wiley.com/doi/abs/10.1029/2019GL084762*

28. Hussain, S. T., Rahman, S. S., Azim, R. A., Haryono, D. & Regenauer-Lieb, K. (2021), 'Multiphase fluid flow through fractured porous media supported by innovative laboratory and numerical methods for estimating relative permeability', *Energy & Fuels* **35**(21), 17372–17388.
URL: *https://doi.org/10.1021/acs.energyfuels.1c01313*

29. Hyman, J. D., Karra, S., Makedonska, N., Gable, C. W., Painter, S. L. & Viswanathan, H. S. (2015), 'dfnworks: A discrete fracture network framework for modeling subsurface flow and transport', *Computers Geosciences* **84**, 10–19.
URL: *https://www.sciencedirect.com/science/article/pii/S0098300415300261*

30. Hyman, J. D., Sweeney, M. R., Frash, L. P., Carey, J. W. & Viswanathan, H. S. (2021), 'Scale-bridging in three-dimensional fracture networks: Characterizing the effects of variable fracture apertures on network-scale flow channelization', *Geophysical Research Letters* **48**(19), e2021GL094400.

31. Karpyn, Z., Grader, A. & Halleck, P. (2007), 'Visualization of fluid occupancy in a rough fracture using micro-tomography', *Journal of Colloid and Interface Science* **307**(1), 181–187.
URL: *https://www.sciencedirect.com/science/article/pii/S0021979706010149*

32. Khosravi, M., Bahramian, A., Emadi, M., Rostami, B. & Roayaie, E. (2014), 'Mechanistic investigation of bypassed-oil recovery during co2 injection in matrix and fracture', *Fuel* **117**, 43–49.
URL: *https://www.sciencedirect.com/science/article/pii/S0016236113009356*

33. Lan, T., Hu, R., Yang, Z., Wu, D.-S. & Chen, Y.-F. (2020), 'Transitions of fluid invasion patterns in porous media', *Geophysical Research Letters* **47**(20), e2020GL089682. e2020GL089682 2020GL089682.
URL: *https://agupubs.onlinelibrary.wiley.com/doi/abs/10.1029/2020GL089682*

34. Landry, C. J., Karpyn, Z. T. & Ayala, O. (2014), 'Relative permeability of homogenous-wet and mixed-wet porous media as determined by pore-scale lattice boltzmann modeling', *Water Resources Research* **50**(5), 3672–3689.
URL: *https://agupubs.onlinelibrary.wiley.com/doi/abs/10.1002/2013WR015148*

35. Leclaire, S., Abahri, K., Belarbi, R. & Bennacer, R. (2016), 'Modeling of static contact angles with curved boundaries using a multiphase lattice boltzmann method with variable density and viscosity ratios', *International Journal for Numerical Methods in Fluids* **82**(8), 451–470.
URL: *https://onlinelibrary.wiley.com/doi/abs/10.1002/fld.4226*

36. Leclaire, S., Parmigiani, A., Malaspinas, O., Chopard, B. & Latt, J. (2017), 'Generalized three-dimensional lattice boltzmann color-gradient method for immiscible two-phase pore-scale imbibition and drainage in porous media', *Phys. Rev. E* **95**, 033306.
URL: *https://link.aps.org/doi/10.1103/PhysRevE.95.033306*

37. Lenormand, R., Touboul, E. & Zarcone, C. (1988), 'Numerical models and experiments on immiscible displacements in porous media', *Journal of Fluid Mechanics* **189**, 165–187.

38. Lenormand, R. & Zarcone, C. (1984), 'Role Of Roughness And Edges During Imbibition In Square Capillaries', pp. SPE–13264–MS.
URL: *https://doi.org/10.2118/13264-MS*

39. Lenormand, R., Zarcone, C. & Sarr, A. (1983), 'Mechanisms of the displacement of one fluid by another in a network of capillary ducts', *Journal of Fluid Mechanics* **135**, 337–353.

40. March, R., Doster, F. & Geiger, S. (2018), 'Assessment of co2 storage potential in naturally fractured reservoirs with dual-porosity models', *Water Resources Research* **54**(3), 1650–1668.
URL: *https://agupubs.onlinelibrary.wiley.com/doi/abs/10.1002/2017WR022159*

41. McClure, J. E., Armstrong, R. T., Berrill, M. A., Schlüter, S., Berg, S., Gray, W. G. & Miller, C. T. (2018), 'Geometric state function for two-fluid flow in porous media', *Phys. Rev. Fluids* **3**, 084306.
URL: *https://link.aps.org/doi/10.1103/PhysRevFluids.3.084306*

42. Ogilvie, S. R., Isakov, E. & Glover, P. W. (2006), 'Fluid flow through rough fractures in rocks. ii: A new matching model for rough rock fractures', *Earth and Planetary Science Letters* **241**(3), 454–465.
URL: *https://www.sciencedirect.com/science/article/pii/S0012821X05008174*

43. Primkulov, B. K., Pahlavan, A. A., Fu, X., Zhao, B., MacMinn, C. W. & Juanes, R. (2019), 'Signatures of fluid–fluid displacement in porous media: wettability, patterns and pressures', *Journal of Fluid Mechanics* **875**, R4.

44. Primkulov, B. K., Pahlavan, A. A., Fu, X., Zhao, B., MacMinn, C. W. & Juanes, R. (2021), 'Wettability and lenormand's diagram', *Journal of Fluid Mechanics* **923**, A34.

45. Reeves, P. C. & Celia, M. A. (1996), 'A functional relationship between capillary pressure, saturation, and interfacial area as revealed by a pore-scale network model', *Water Resources Research* **32**(8), 2345–2358.
URL: *https://agupubs.onlinelibrary.wiley.com/doi/abs/10.1029/96WR01105*

46. Song, W., Prodanovic, M., Santos, J. E., Yao, J., Zhang, K. & Yang, Y. (2023), 'Upscaling of Transport Properties in Complex Hydraulic Fracture Systems', *SPE Journal* **28**(03), 1026–1044.
URL: *https://doi.org/10.2118/212849-PA*

47. Tsuji, T., Jiang, F. & Christensen, K. T. (2016), 'Characterization of immiscible fluid displacement processes with various capillary numbers and viscosity ratios in 3d natural sandstone', *Advances in Water Resources* **95**, 3–15. Pore scale modeling and experiments.
URL: *https://www.sciencedirect.com/science/article/pii/S0309170816300550*

48. Wang, Y., Vuik, C. & Hajibeygi, H. (2022), 'Co2 storage in deep saline aquifers: impacts of fractures on hydrodynamic trapping', *International Journal of Greenhouse Gas Control* **113**, 103552.
URL: *https://www.sciencedirect.com/science/article/pii/S1750583621003030*

49. Xu, Z., Liu, H. & Valocchi, A. J. (2017), 'Lattice boltzmann simulation of immiscible two-phase flow with capillary valve effect in porous media', *Water Resources Research* **53**(5), 3770–3790.
URL: *https://agupubs.onlinelibrary.wiley.com/doi/abs/10.1002/2017WR020373*

50. Yi, J., Xing, H., Wang, J., Xia, Z. & Jing, Y. (2019), 'Pore-scale study of the effects of surface roughness on relative permeability of rock fractures using lattice boltzmann method', *Chemical Engineering Science* **209**, 115178.
URL: *https://www.sciencedirect.com/science/article/pii/S0009250919306694*

51. Zhang, C., Oostrom, M., Wietsma, T. W., Grate, J. W. & Warner, M. G. (2011), 'Influence of viscous and capillary forces on immiscible fluid displacement: Pore-scale experimental study in a water-wet micromodel demonstrating viscous and capillary fingering', *Energy & Fuels* **25**(8), 3493–3505.
URL: *https://doi.org/10.1021/ef101732k*

52. Zhao, B., MacMinn, C. W. & Juanes, R. (2016), 'Wettability control on multiphase flow in patterned microfluidics', *Proceedings of the National Academy of Sciences* **113**(37), 10251–10256.
URL: *https://www.pnas.org/doi/abs/10.1073/pnas.1603387113*

53. Zhou, C.-B., Chen, Y.-F., Hu, R. & Yang, Z. (2023), 'Groundwater flow through fractured rocks and seepage control in geotechnical engineering: Theories and practices', *Journal of Rock Mechanics and Geotechnical Engineering* **15**(1), 1–36.
URL: *https://www.sciencedirect.com/science/article/pii/S1674775522002013*

List of Figures

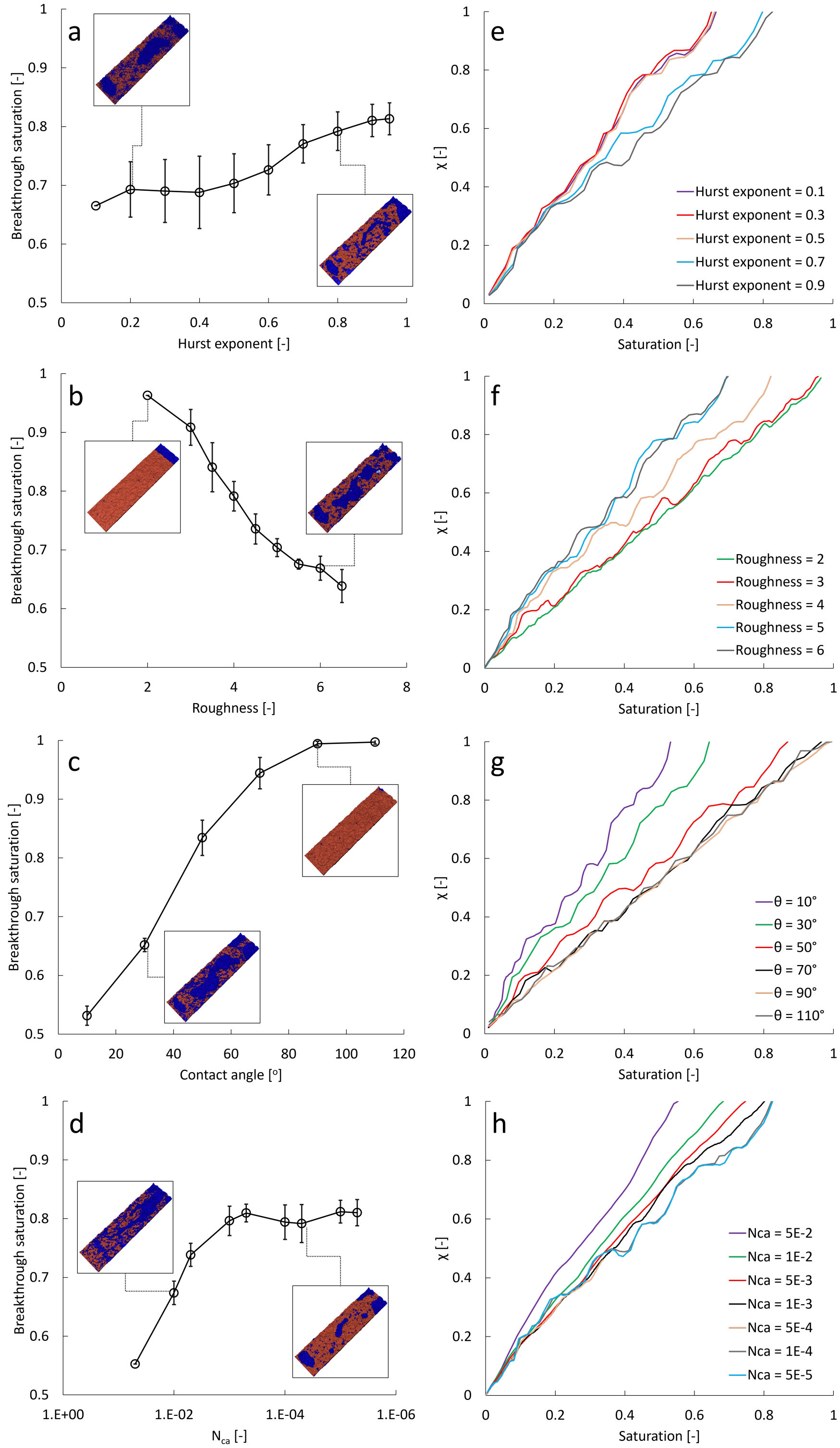

Figure 1: Breakthrough saturation and front migration profiles for different fracture and flow parameters. All data points reported for the BTS values are average of three seeds used for generating fracture realizations and standard deviation is estimated from this triplicate information. For tracking the front migration, normalized front tip length (χ) is obtained for the front tip length at any given saturation divided by the total number of lus in the direction of flow (512 lus for all fractures considered in this work). Here, the normalized front tip lengths are shown only for seed 1.

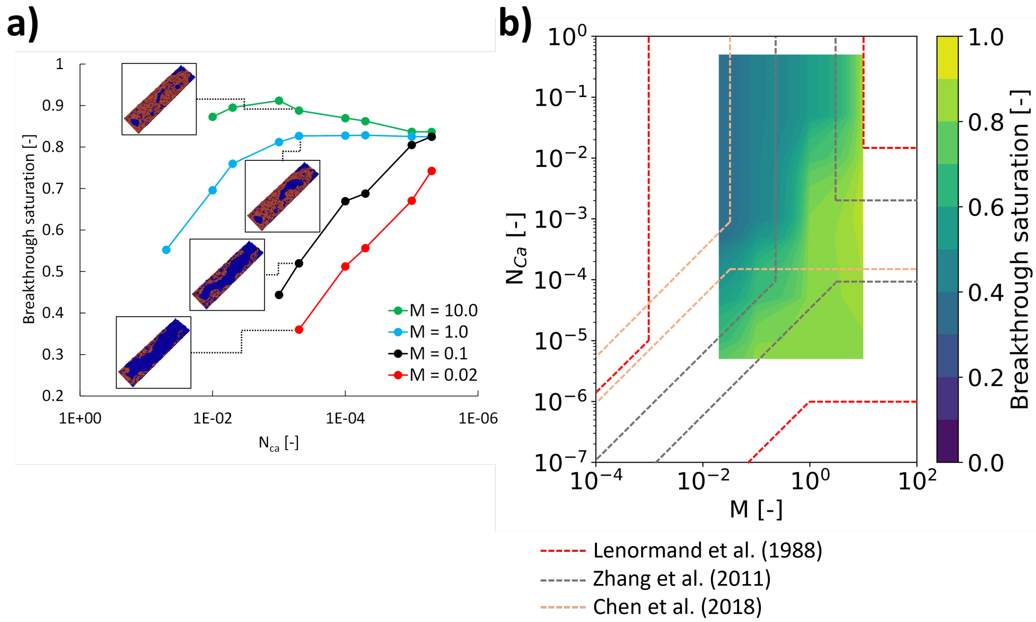

Figure 2: (a) Breakthrough saturation for different viscosity ratios and capillary numbers. (b) Phase diagram showing different displacement regimes in the same fracture realization. Boundaries for viscous fingering, capillary fingering, and stable displacement from the Lenormand and Lenormand-type diagrams are overlain on the plot (Lenormand et al. (1988), Zhang et al. (2011), Chen, Wu, Fang & Hu (2018). The region bounded in the top-right corresponds to stable displacement while the region bounded by the viscosity ratio axis corresponds to capillary fingering. Similarly, the region bounded by the capillary number axis corresponds to the viscous fingering. The following fracture and flow properties were fixed in these figures rms roughness = 4, Hurst exponent = 0.7, seed = 1, and contact angle = 45°.

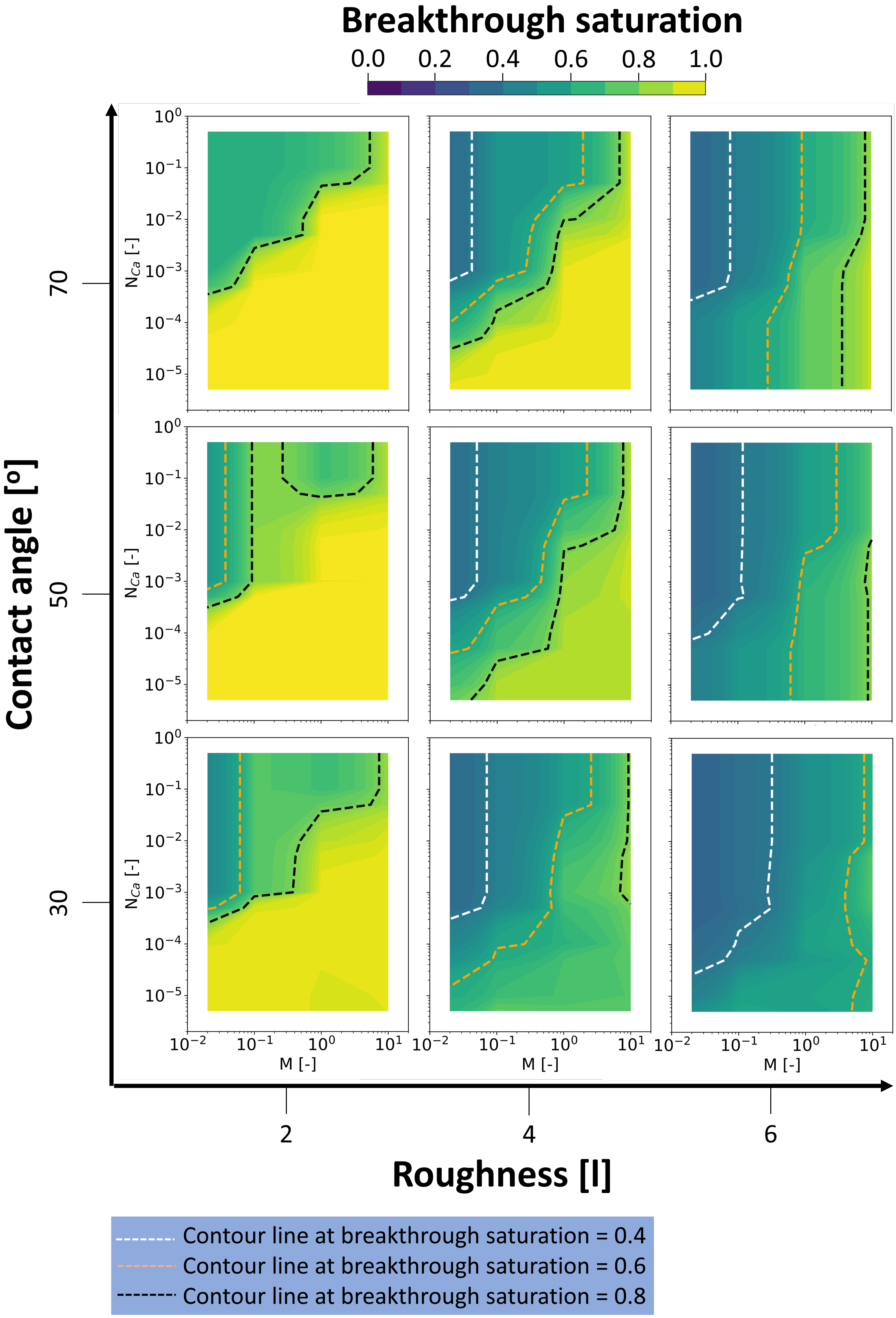

Figure 3: Displacement pattern phase diagrams for different fractures. Three different rms roughness values (2, 4, and 6) and three different contact angle cases (30°, 50°, and 70°) are considered for the full range of capillary numbers and viscosity ratios discussed previously in Figure 2b. All simulations discussed here are for seed one and the Hurst exponent was fixed at 0.7.